A SQUID NDE MEASUREMENT MODEL USING BEM

Mr. A.P. Ewing[1,2],
Dr. T.A. Cruse[1], and
Dr. J.P. Wikswo, Jr.[2]

[1]Dept. of Mechanical Engineering
[2]Dept. of Physics and Astronomy
Vanderbilt University
Nashville, TN USA

INTRODUCTION

As the commercial and military aircraft fleets age, additional resources are required to ensure their airworthiness. As the aircraft become older, the more likely they are to develop structural damage that may lead to unscheduled repairs or, in the worst case, accidents. Fatigue and corrosion are the two main causes of structural damage in aging aircraft and this research examines the use of a Superconducting QUantum Interference Device (SQUID) as a tool for Nondestructive Evaluation (NDE) to detect and characterize these aging aircraft problems. The primary advantage of using SQUIDs in NDE over other techniques is the ability to detect second layer cracks and corrosion commonly found in aircraft structures.

In general, verification of a NDE method means demonstrating, through experiment and/or calculations, the ability to distinguish signal from noise for the flaw types and sizes and instrument/flaw configurations expected in the actual inspection. A common approach to quantify and validate the capabilities of an inspection technique is to conduct a probability of detection (POD) analysis. There are basically two ways to conduct this type of analysis. The first is experimentally, which requires a large number of samples with a range of flaw characteristics being examined by several inspectors. The second is analytically, which requires construction of a model to simulate the inspection process which is run for a range of samples and testing conditions. Due to the large number of parameters defining a method, experimental results alone are usually inadequate but are still required to describe system parameters that cannot be modeled analytically. With mathematical modeling, the response of the measurement system to the anomalies of interest (e.g., cracks, corrosion, and voids) can be simulated if enough is known about the

Review of Progress in Quantitative Nondestructive Evaluation, Vol 17
Edited by D.O. Thompson and D.E. Chimenti, Plenum Press, New York, 1998

field-flaw interaction that generates the response function. Due to the complexity of the mathematics of these interactions, idealized models are normally used but these still provide sensitivity analysis information useful in evaluating the inspection technique.

The following is the development of a measurement model simulating the scanning of a SQUID over a sample containing a crack. We model a closed crack through a special development of boundary integral equations, which is used to calculate corresponding magnetic fields, simulating what the SQUID instrument measures. The measurement model will be used later in a POD analysis.

THEORY

SQUID Measurement Models

Of the several NDE techniques available to the SQUID user, dc-current injection was used in this research since the current distributions produced are similar to the planar ac eddy currents produced by sheet inducers which are proposed for a field instrument. Also, existing BIE programs can be modified to model dc-current injection which provides the basis for an accurate measurement model. Injecting a uniform dc-current in the specimen causes the current to be parallel to the specimen surface under the pickup coil. The associated magnetic field is mostly tangential to the plate surface for scans located centrally and with small lift-off distances. A flaw in the specimen will perturb the current distribution and produce a vertical magnetic field component that can then be detected by the SQUID. When the SQUID is scanned two-dimensionally over the sample, a magnetic map is produced, revealing a flaw signature that commonly has a dipolar shape (Fig. 1).

Boundary Integral Equation (BIE) Measurement Model

Boundary Integral Equations are the basis for our SQUID NDE measurement model. The BIE formulation solves for the potential problem of a dc-current carrying plate containing a fastener hole with a crack emanating from one side. From these potentials, the magnetic field can be calculated through the law of Biot and Savart. The BIE approach uses a special formulation incorporating the crack geometry into the Green's function, thereby eliminating the need to model it as part of the boundary. It is important to point out that this modeled crack is a closed crack, as compared to a slot having finite width. A slot-type crack (an approximation of a fatigue crack) would not require the special Green's function formulation and could just be modeled as part of the boundary.

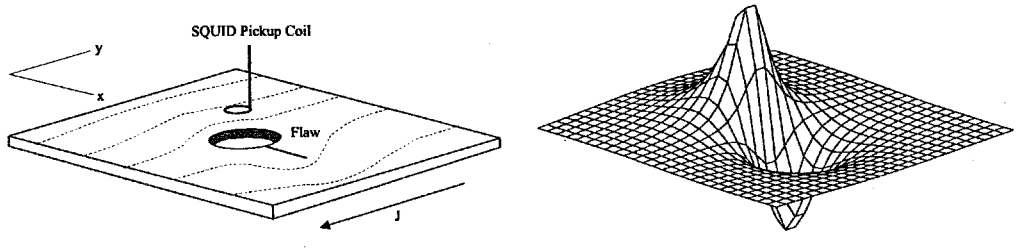

Figure 1. 2-D scan over sample and resulting magnetic field map.

Details of the boundary integral equation development are provided in [1] and the following discussion summarizes the application to the electromagnetic problem. The Biot-Savart law [2] can be used to determine the z-component of the magnetic field over a plate, with thickness h and conductivity σ, by integration of the tangential derivative of the electric scalar potential, V, over the crack (Γ) and other boundaries (S)

$$B_z(c) = -\frac{\mu_0 \sigma h}{4\pi} \int_{S+\Gamma} \frac{\vec{\nabla} V \cdot \hat{t}}{r(c,Q)} ds(Q). \tag{1}$$

The BIE program calculates $V_t = \vec{\nabla} V \cdot \hat{t}$ as a piecewise linear result since V(Q) is piecewise quadratic. Therefore, V_t can be rewritten for the line segment along S on the integration boundary as $V_t(Q) = b_1 + b_2 s$. This is done for all boundary surfaces except for the crack surface (Γ). Substituting this linear relationship into the integral for $B_z(c)$, we obtain the contribution to the magnetic field at point c due to all boundaries except for Γ

$$B_z(c)\big|_S = -\frac{\mu_0 \sigma h}{4\pi} \int_S \frac{b_1 + b_2 s}{r(c,Q)} ds(Q). \tag{2}$$

For the non-crack boundaries, this integration is fairly straightforward taking into account the geometrical relationship between the pickup coil and the boundary segments. Carrying out the integration, we obtain the following summation over all non-crack boundary segments on S

$$\mathrm{B_z(c)} = \sum_{\mathrm{n}} -\frac{\mu_0 \sigma h D}{4\pi} \left[B_1 \ln\left\{ \tan\left(\frac{\pi}{4} + \frac{\theta}{2} \right) \right\} + \frac{b_2}{\cos\theta} \right]_{\theta_1}^{\theta_2}, \tag{3}$$

where θ_1 and θ_2 correspond to the angles associated with each endpoint of the segment as the summation moves in a positive sense around the boundary (material on left).

For the crack (length a), the singular behavior of V_t at the crack tip requires numerical integration to evaluate the magnetic field contribution of the crack. Values of V_t will be evaluated near the upper and lower crack surfaces using the BIE program and then the magnetic field will be calculated through a numerical integration of the previously stated Biot-Savart relation (Eq. 1). The series expansion of V_t is given by [3]

$$V_t = \frac{f_1(x)}{\sqrt{x^2 - a^2}} + f_2(x), \tag{4}$$

where $f_1(x)$ and $f_2(x)$ are analytic functions. The first term contains the discontinuity at

the crack tip while the second term is needed to match far field boundary conditions. On the crack surface (Γ) this can be rewritten as

$$\begin{aligned} V_t|_\Gamma &= \frac{if_1(x)}{\sqrt{a-x}\sqrt{a+x}} + f_2(x) \\ &= \frac{1}{\sqrt{R}}\frac{if_1(x)}{\sqrt{a+x}} + f_2(x) \\ &= \frac{1}{\sqrt{R}} iF_1(x) + f_2(x) \end{aligned} \quad , \tag{5}$$

where R is the distance measured from the crack tip. Equation 5 is well behaved except at the crack tip. For the region near the crack tip, the behavior of V_t is known to follow

$$V_t = -\frac{K^+}{\sqrt{2\pi R}} \sin\frac{\beta}{2}, \tag{6}$$

where K^+ is the potential intensity factor (PIF) of the crack. Note that at $R = 0$ (crack tip), $V_t = \infty$. The sine term reflects a geometrical dependence of V_t on β, the angle measured from the crack tip to the evaluation point and results in either a plus or minus sign multiplier when integrating on the crack surface. By combining equations (5) and (6), we can express the term multiplying the singular term, in terms of the PIF

$$F_1(a) = \mp\frac{K^+}{\sqrt{2\pi}} - f_2(a). \tag{7}$$

With the function value at the crack tip now defined, we can continue with the numerical integration development.

Numerical Integration

Numerical integration over the crack is accomplished through discretization of the crack boundary into elements. By utilizing a coordinate transformation, V_t can be expressed in terms of nodal values and interpolation functions (shape functions) of an intrinsic

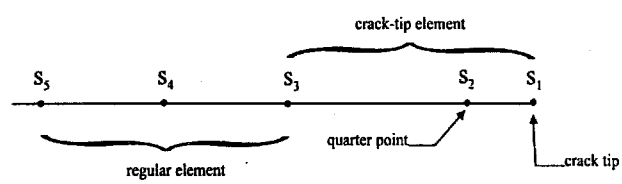

Figure 2. Discretization of crack into elements.

coordinate ξ. Once mapped into ξ-space, Gaussian quadrature numerical integration can be used to evaluate the integral. This formulation uses quadratic interpolation functions $N_m(\xi)$ which requires three nodes per boundary element. The crack is modeled with one crack-tip element containing the crack-tip node and one regular element (Fig. 2). The regular element is a straight forward application of the interpolation functions but the crack-tip element will use a quarter-point formulation [4] to map the singular behavior at the crack tip.

The general form of the quadratic interpolation functions used to map the function to be integrated into the ξ-space are

$$\begin{aligned} N_1(\xi) &= \frac{1}{2}\xi(\xi-1) \\ N_2(\xi) &= 1-\xi^2 \\ N_3(\xi) &= \frac{1}{2}\xi(\xi+1). \end{aligned} \tag{8}$$

The coordinate transformation into ξ-space of the integral results in the following sum

$$\int_\Gamma F(s)ds \rightarrow \sum_{k=1}^{3}\int_{-1}^{+1} N_k(\xi)F_k J(s,\xi)d\xi\,, \tag{9}$$

where F_k is the value of the function at the *kth* node and J is the Jacobian of the mapping that accounts for the spatial scaling associated with the mapping,

$$J(s,\xi) = \frac{ds}{d\xi} = \sum_{k=1}^{3}\frac{dN_k}{d\xi}s_k\,. \tag{10}$$

For those boundary elements that do not contain the crack tip, the resulting integral for B_z becomes

$$\begin{aligned} B_z|_\Gamma &= -\frac{\mu_0\sigma h}{4\pi}\int_0^L\left(\frac{V_t(s)}{r(s)}\right)ds \\ &= -\frac{\mu_0\sigma h}{4\pi}\int_{-1}^{+1}\left[N_1(\xi)\left(\frac{V_t(s)}{r(s)}\right)_{s_1} + N_2(\xi)\left(\frac{V_t(s)}{r(s)}\right)_{s_2} + N_3(\xi)\left(\frac{V_t(s)}{r(s)}\right)_{s_3}\right]J(s,\xi)d\xi \\ &= -\frac{\mu_0\sigma h}{4\pi}\frac{L}{2}\int_{-1}^{+1}\left[N_1(\xi)\left(\frac{V_t(0)}{r(0)}\right) + N_2(\xi)\left(\frac{V_t(L/2)}{r(L/2)}\right) + N_3(\xi)\left(\frac{V_t(L)}{r(L)}\right)\right]d\xi, \end{aligned} \tag{11}$$

which can now be numerically integrated using Gaussian quadrature techniques.

For the crack-tip element on the upper crack surface, the standard mapping to ξ-space needs to be modified to accommodate the $1/\sqrt{s}$ behavior of $V_t(s)$ at the crack tip. The general approach is to split the $V_t(s)$ term into a singular term multiplied by a non-singular coefficient. The form of $V_t(s)$ follows from Eq. (5),

$$V_t(s)\big|_\Gamma = \frac{if(s)}{\sqrt{s}\sqrt{2L-s}} = \frac{1}{\sqrt{s}}F_1(s). \tag{12}$$

To map $V_t(s)$ into ξ-space, the singular term uses an inverse mapping relationship and the non-singular term uses the quadratic shape functions. For the inverse mapping, the $1/\sqrt{s}$ behavior is represented by placing the midnode of the quadratic element at the quarter point location,

$$\xi = -1 + 2\sqrt{\frac{s}{L}} \quad \rightarrow \quad \frac{1}{\sqrt{s}} = \frac{2}{\sqrt{L}}\frac{1}{(\xi+1)}. \tag{13}$$

The Jacobian, J, is given by

$$J = \frac{ds}{d\xi} = \frac{L}{2}(1+\xi). \tag{14}$$

Note that at the s=0 (ξ=-1) point the Jacobian also equals zero. This characteristic is important when evaluating the integral of the mapped function. Therefore, the B_z contribution due to the crack-tip element on the upper crack surface is as follows

$$\begin{aligned} B_z\big|_\Gamma &= -\frac{\mu_0 \sigma h}{4\pi}\int \frac{V_t(s)}{r(s)}ds = -\frac{\mu_0 \sigma h}{4\pi}\int_0^L \frac{1}{\sqrt{s}}\left(\frac{F(s)}{r(s)}\right) \\ &= -\frac{\mu_0 \sigma h}{4\pi}\int_{-1}^{+1}\frac{2}{\sqrt{L}}\frac{1}{(\xi+1)}\left[N_1(\xi)\left(\frac{F(s)}{r(s)}\right)_{s_1} + N_2(\xi)\left(\frac{F(s)}{r(s)}\right)_{s_2} + N_3(\xi)\left(\frac{F(s)}{r(s)}\right)_{s_3}\right]\frac{L}{2}(\xi+1)d\xi \\ &= -\frac{\mu_0 \sigma h}{4\pi}\sqrt{L}\int_{-1}^{+1}\left[N_1(\xi)\left(\frac{F(s_1)}{r(s_1)}\right) + N_2(\xi)\left(\frac{F(s_2)}{r(s_2)}\right) + N_3(\xi)\left(\frac{F(s_3)}{r(s_3)}\right)\right]d\xi . \end{aligned} \tag{15}$$

Note that as ξ→-1, the singularity term (ξ+1 in denominator) goes to infinity but is canceled by the Jacobian term (ξ+1 in numerator) going to zero, thereby making the overall function finite in the mapped space. All values of F, r, and s are known except for F at the crack tip node which has the singularity. But at the crack tip the value of the function is related to the PIF (Eq. 7), in that $F(s_1) = K^+/\sqrt{2\pi}$.

EXPERIMENTAL VALIDATION

One of the validation experiments used a 5 mA dc-current injected into a 100 mm × 150 mm × 0.03 mm copper clad circuit board containing a 15 mm × 0.03 mm slot cut with a scalpel. Although this setup does not provide completely uniform current injection across the sample (transverse to the slot) due to the point source electrodes, the region around the centrally located slot should be relatively uniform. Some discrepancy is expected due to the fact that the scalpel-cut slot has width rather than the closed crack used in the measurement model. Direct amplitude comparison is not possible and, therefore will require a scaling factor between the measured magnetic field and the calculated magnetic field. Magnetic field shape characteristics (matching of peaks and valleys) will determine the accuracy of the measurement model.

Figure 3 shows a comparison of the centerline profiles, after scaling, of the magnetic field maps obtained by experimental measurement (solid line) and from the measurement model calculation (dashed line). The two are in very good agreement with respect to the overall profile shape. Since the calculated field is scaled, a difference between the model and experiment would show up as a mismatch of the profiles at either the edge or the crack depending on which was used as reference in the scaling.

SUMMARY

This research is directed towards the use of a Superconducting QUantum Interference Device (SQUID) as a tool for Nondestructive Evaluation (NDE) to detect and characterize damage associated with aging aircraft. The primary advantage of using SQUID's in NDE over other techniques is the ability to detect second layer cracks and corrosion commonly found in aircraft structures. In order to quantify and validate the capabilities of SQUID's in this role, we are beginning a probability of detection (POD) analysis. This paper introduces the analytical model that will be used to conduct this analysis.

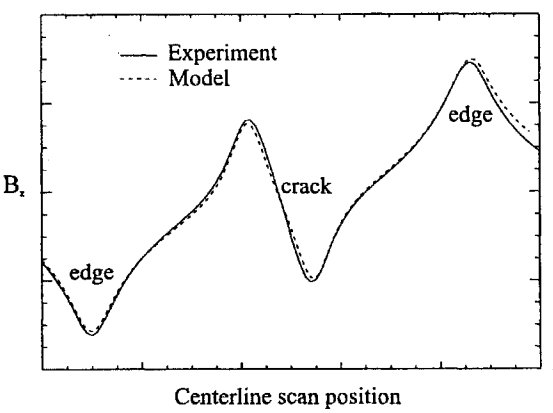

Figure 3. Magnetic field map centerline profiles comparison.

The approach has been to develop a measurement model simulating the scanning of a SQUID over a sample containing a crack. Boundary integral equations, using a special Green's function incorporating the crack, are used to solve the potential problem. This special formulation eliminates the necessity of fine meshes at the crack tips normally required for comparable approaches. From the BIE potential solution, the magnetic field above the sample can be calculated through numerical integration techniques of the Biot-Savart law. Specific techniques, such as quadratic interpolation functions and a quarter-point formulation, were required to accommodate the singular behavior at the crack tip. Preliminary comparisons with experimental results show good agreement with the measurement model and validation will continue, as more experimental data sets become available.

ACKNOWLEDGEMENTS

This work is supported by AFOSR Grant F49620-93-0268 and ASSERT Grant F49620-94-1-0369.

REFERENCES

1. Cruse, T.A., Ewing, A.P., "Special Green's Function Formulation of Laplace's Equation for EM Application", Manuscript in preparation.
2. Griffiths, D.J., Introduction to Electrodynamics Prentice-Hall, Inc. 1981 p. 185.
3. Westergaard, H.M., "Bearing Pressures and Cracks", Journal of Applied Mechanics, Vol. 61, pp. A49-A53. 1939.
4. Burnett, D.S., Finite Element Analysis – From Concepts to Applications Addison-Wesley Publishing Company, 1987 pp. 305-327.